Research Square

Preprints are preliminary reports that have not undergone peer review.
They should not be considered conclusive, used to inform clinical practice,
or referenced by the media as validated information.

Evaluation of ASTER and Landsat-9 OLI remote sensing data for ophiolite mapping and preliminary chromium prospectivity assessment in the Tekirova–Kemer– Kumluca region, southern Türkiye

Mamadou Traore

matraba77@gmail.com

University of Bangui

Sezer UNAL

Akdeniz University

Ulaş Inan SEVIMLI

Antalya IVF

Mustafa Gurhan YALCIN

Akdeniz University

Jonas Didero TAKODJOU WAMBO

Lamar University

Ozgur AKTURK

Akdeniz University

Research Article

Keywords: ophiolite mapping, ASTER, Landsat-9 OLI, Support Vector Machine, podiform chromite, chromium prospectivity

Posted Date: July 14th, 2026

DOI: https://doi.org/10.21203/rs.3.rs-10210155/v1

License: This work is licensed under a Creative Commons Attribution 4.0 International License.
Read Full License

Additional Declarations: No competing interests reported.

Evaluation of ASTER and Landsat-9 OLI remote sensing data for ophiolite mapping and preliminary chromium prospectivity assessment in the Tekirova–Kemer–Kumluca region, southern Türkiye

Mamadou TRAORE[1] *, Sezer UNAL[2] *, Ulaş Inan SEVIMLI[3], Mustafa Gurhan YALCIN [2]*, Jonas Didero TAKO-DJOU WAMBO[4] and Ozgur AKTURK[2]

[1] Department of Earth Sciences, Faculty of Sciences, Bangui University, Bangui, Central African Republic.; matraba77@gmail.com;
[2] Akdeniz University, Engineering Geology, 07058, Antalya, Turkey;
[3] ASAT Antalya, Turkey; usevimli@gmail.com
[4] Department of Earth and Space Sciences, Lamar University, Beaumont, TX 77710, USA

* Correspondence: Mamadou Traore (matraba77@gmail.com); Mustafa Gürhan Yalçın (gurhanyalcin@akdeniz.edu.tr); Sezer UNAL[2] *,

Abstract

Podiform chromite mineralization housed within supra-subduction zone ophiolites represents a critical economic resource, yet precise lithological mapping in rugged terrains remains logistically challenging due to inaccessibility and the coarse resolution of existing geological maps. This study addresses the necessity for high-resolution discrimination of ultramafic units in the Tekirova–Kemer–Kumluca ophiolite complex, southern Türkiye, to establish a robust preliminary chromium prospectivity framework. By integrating multispectral datasets from Landsat-9 OLI and ASTER, we applied a suite of spectral enhancement techniques, specifically Decorrelation Stretch (DS), Band Ratio (BR) compositing, and Principal Component Analysis (PCA), to isolate the unique spectral signatures of dunite, harzburgite, and serpentinized zones. The efficacy of these methods was validated against extensive field sampling and petrographic analysis. Our results demonstrate that the ASTER Band Ratio (B5/B8, B4/B2, B5/B4) offers superior discrimination capabilities for serpentinized harzburgites, primarily due to its sensitivity to Mg-OH absorption features in the SWIR region. Furthermore, the Support Vector Machine (SVM) classification achieved an overall accuracy of 90% (Kappa = 0.87), outperforming the Maximum Likelihood baseline tested on the same independent validation set. The integration of these remote sensing products with field-based geochemical analysis (n = 23 samples, XRF) delineated lithological domains permissive for podiform chromite mineralization, showing strong spatial correspondence between mapped serpentinized ultramafic units and Cr_2O_3 enrichment (Cr_2O_3-MgO Pearson correlation $r = 0.92$, $p < 0.001$). These findings suggest that the proposed multi-sensor integration approach provides a cost-effective and scalable protocol for mineral exploration in geologically complex and vegetative ophiolitic belts.

Keywords: ophiolite mapping; ASTER; Landsat-9 OLI; Support Vector Machine; podiform chromite; chromium prospectivity

1. Introduction

Ophiolite complexes represent fragments of ancient oceanic lithosphere obducted onto continental margins during subduction and collision processes, primarily in supra-subduction zone settings (Zoheir et al. 2019; Amer et al. 2010). These sequences are of significant geological and economic interest due to their association with podiform chromite mineralization, which occurs as lens-shaped chromitite bodies within ultramafic mantle sections, particularly dunites and harzburgites (Arai and Yurimoto 1994; Bağcı 2004). Chromite deposits in such environments form through melt-rock interaction and partial melting in the mantle wedge, resulting in high-Cr_2O_3 concentrations that are economically viable when concentrated (Zoheir et al. 2019; Amer et al. 2010). In Türkiye, the Tauride ophiolites, including the Tekirova–Kemer–Kumluca region within the Antalya Complex, host well-documented examples of these features, yet regional geological maps remain generalized, often failing to resolve internal lithological variations and spatial relationships with chromium enrichment (Bağcı and Parlak 2009; Bilgilioğlu 2024; Çelik 2007).

Remote sensing has emerged as a powerful tool for lithological mapping in rugged, inaccessible terrains where traditional field-based approaches are limited by topography and vegetation cover. In particular, selecting optimal band combinations and robust classification models remains a critical challenge in structurally complex and moderately vegetation-covered regions (Chen et al. 2023). Multispectral sensors such as the Advanced Spaceborne Thermal Emission and Reflection Radiometer (ASTER) and Landsat series provide diagnostic spectral responses from rock-forming minerals, particularly Fe^{2+}-bearing silicates in ultramafic rocks and hydroxyl-bearing alteration products resulting from

serpentinization (Zoheir et al. 2019; Amer et al. 2010). ASTER's short-wave infrared (SWIR) bands offer enhanced sensitivity to mineralogical features, while Landsat sensors provide consistent global coverage and improved radiometric resolution in recent iterations. Previous studies have successfully applied band ratio techniques, Principal Component Analysis (PCA), and Minimum Noise Fraction (MNF) transformations to discriminate ophiolitic units in similar settings as well as other economic mineralization styles including alluvial gold and carbonate-hosted Pb-Zn zones (Traore et al. 2020, 2022). However, many of these efforts rely on qualitative image interpretation or single-sensor approaches, with limited use of supervised machine-learning classification, independent accuracy assessment, or integration with field geochemical constraints.

The integration of multiple sensors—such as Landsat-9 Operational Land Imager (OLI) and ASTER—offers complementary advantages: Landsat-9's superior signal-to-noise ratio and radiometric stability complement ASTER's SWIR mineralogical detail, enabling more robust lithological discrimination (Çelik and Delaloye 2003; Carvalho et al. 2025; Badr et al. 2026b). Despite these advances, few studies have developed novel band-ratio combinations tailored to specific ultramafic spectral signatures or combined them with Support Vector Machine (SVM) classification for reproducible regional mapping [14,15,16,17;45]. Although the mineralogical sensitivity of Landsat and ASTER sensors is well known in the remote sensing literature, there is still a significant gap in the development of novel band ratio combinations specific to ultramafic rocks and their integration with machine learning methods such as SVM (Support Vector Machines). In this context, machine learning algorithms have been used in the investigation of podiform chromite deposits (Eskandari et al. 2023). Similarly, a regional mapping approach has been observed by integrating multi-sensor data with field-validated data to determine the boundaries of ophiolitic complexes in Egypt (Badr et al. 2026a). Moreover, while chromium prospectivity in ophiolites is well-established, remote sensing applications rarely link classified ultramafic domains to quantitative geochemical data, leaving a gap in validating permissive lithological zones for podiform chromite.

This study addresses these limitations by proposing an integrated multispectral framework for detailed ophiolite mapping in the Tekirova–Kemer–Kumluca region. The approach combines Landsat-9 OLI and ASTER data with spectral enhancements, including a newly proposed ASTER band-ratio composite (5/8, 4/2, 5/4) targeting Mg-OH and Al–OH absorption features, followed by supervised SVM classification and validation against independent points. Field geochemical analysis of fresh ultramafic samples provides ground-truth constraints on chromium distribution. The principal results demonstrate high classification accuracy (Kappa 0.87) and strong spatial correspondence between mapped ultramafic units and Cr_2O_3 enrichment, offering a transferable methodology for regional-scale ophiolite mapping and preliminary chromium prospectivity assessment in similar tectonic settings.

2. Geological Setting

The Tekirova–Kemer–Kumluca region is located in southern Turkey and forms part of the Antalya Complex within the Neotethyan Alpine–Himalayan orogenic belt (Fig. 1). The regional geological framework has been constrained by previous tectono-stratigraphic studies (Juteau 1975; Honarmand et al. 2024; Çelik and Chiaradia 2008; Dilek et al. 1999) .

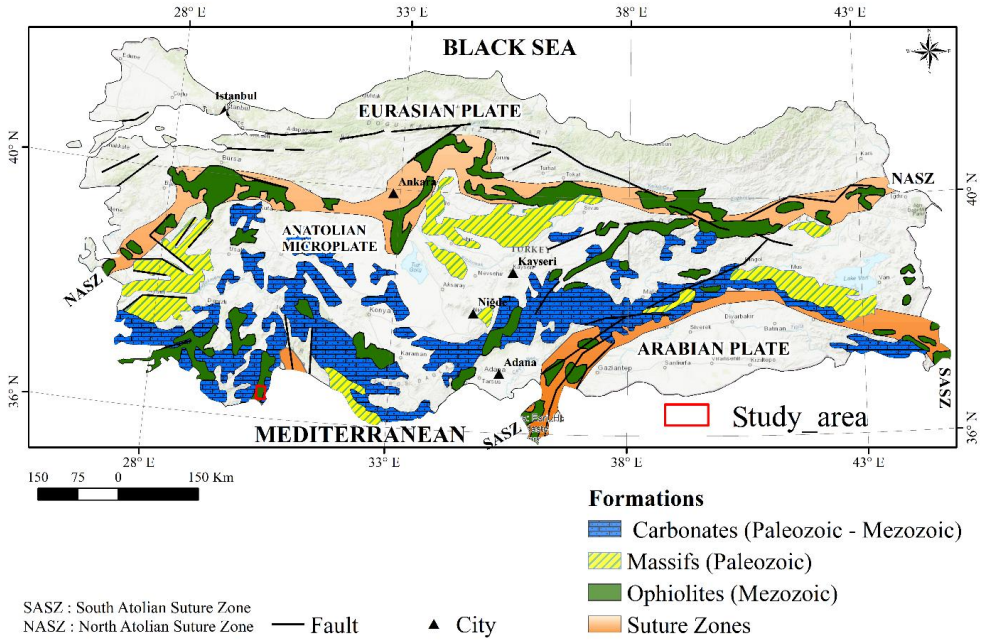


Fig. 1 Distribution of ophiolites and related chromite occurrences in Türkiye (modified after Engin 1985).

The dominant geological unit in the study area is the Tekirova ophiolite, which consists of mantle-derived ultramafic rocks, including harzburgite, dunite, and variably serpentinized peridotite, locally overlain by gabbroic and volcanic units (Fig. 2). These ophiolitic rocks are tectonically juxtaposed against carbonate and clastic sedimentary units of the Beydağları platform. The Tauride ophiolites are widely interpreted as remnants of Neotethyan oceanic lithosphere emplaced during Late Cretaceous subduction and subsequent continental collision processes (Robertson 1998; Robertson and Woodcock 1982; Gabr et al. 2010; Gad and Kusky 2007; González-Jiménez et al. 2014).

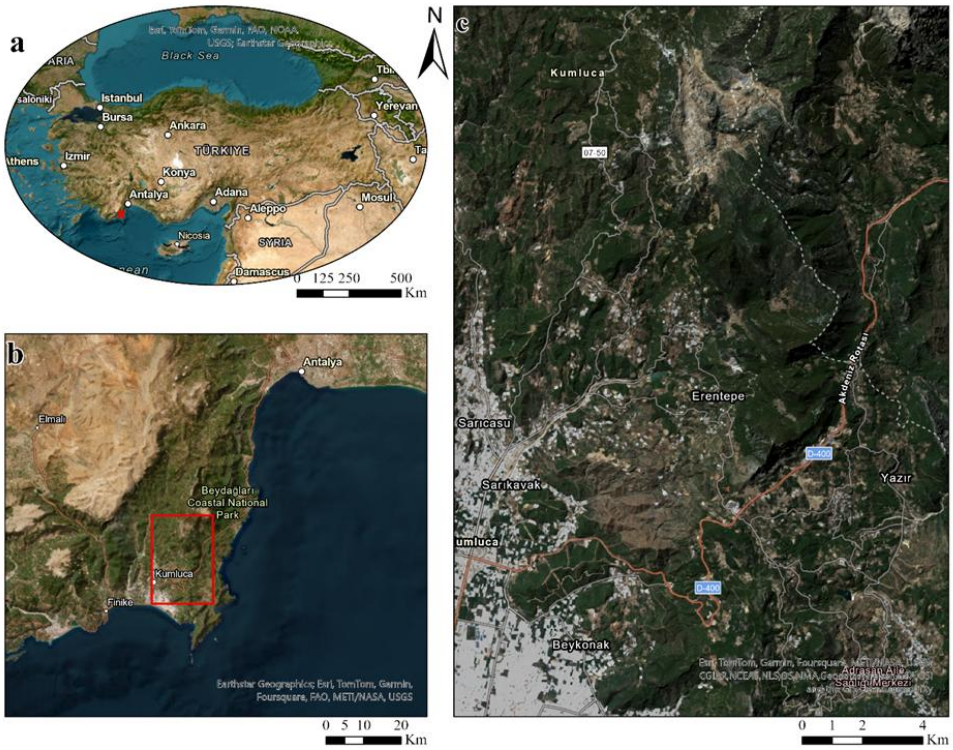


Fig. 2 Location of the study area: (a) national-scale context within Türkiye; (b) regional geological framework of southern Turkey highlighting the Antalya Complex; (c) detailed view of the Tekirova–Kemer–Kumluca study area. Geological framework modified after Güneş 2018; basemap imagery from Esri.

Podiform chromite mineralization, a characteristic feature of supra-subduction zone ophiolites, occurs within dunite lenses and zones of intense serpentinization throughout the region [26, 4]. Although existing geological maps provide an essential regional framework (Güneş 2018), they remain generalized at the scale required to resolve detailed lithological boundaries and internal heterogeneity within the ophiolite (Fig. 3). The geological complexity and rugged topography of the area make it an ideal test site for evaluating integrated multispectral remote sensing approaches for detailed lithological mapping.

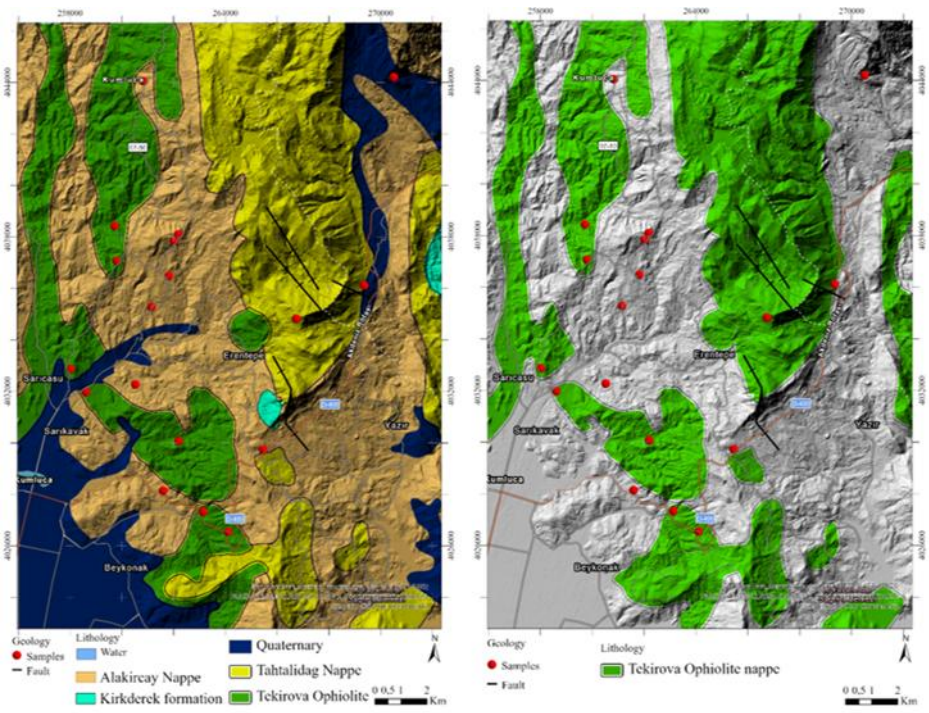


Fig. 3 Geological map of the study area (modified after Güneş 2018). The map was georeferenced and digitized in ArcGIS Pro, with the Tekirova ophiolite unit manually delineated. Satellite imagery is used solely as a cartographic basemap.

3. Materials and Methods

3.1. Satellite Data and Preprocessing

This study utilized multispectral data from the Advanced Spaceborne Thermal Emission and Reflection Radiometer (ASTER) and Landsat-9 Operational Land Imager (OLI) to exploit complementary spectral ranges (Table 1). A cloud-free ASTER Level-1T scene (Product ID: AST_L1T_00308222006085142_20150515204010_83662) was acquired on 19 July 2006 and a Landsat-9 OLI scene (Product ID: LC09_L1TP_179037_20220720_20230416_02_T1) acquired on 20 July 2022 were downloaded from the USGS EarthExplorer portal.

Both datasets were atmospherically corrected to surface reflectance using the Dark Object Subtraction (DOS) method (Chavez 1988). Minimum digital number (DN) values were extracted from deep Mediterranean Sea water bodies: ASTER bands 1–3 (DN = 18, 22, 15) and Landsat-9 bands 2–7 (DN = 12, 8, 6, 4, 3, 2). Topographic correction applied the C-correction method [28;41] using a 30-m SRTM DEM to mitigate illumination effects in mountainous terrain. ASTER SWIR bands were resampled to 30 m via cubic convolution to match Landsat-9 resolution. Geometric alignment used 25 ground control points, achieving an RMS error of 0.38 pixels (<12 m horizontal accuracy), and all data were projected to UTM Zone 36N (WGS84 datum).

To address the 16-year temporal gap between the 2006 ASTER scene and the 2022 Landsat-9 OLI scene, the temporal stability of land cover over the ophiolite outcrops was qualitatively assessed. Visual inspection of NDVI surfaces derived from both acquisitions, together with high-resolution Esri basemap imagery, indicates that vegetation cover and rock exposure remained largely stable over the ultramafic outcrops, consistent with the arid to semi-arid climate and rugged topography of the Tekirova–Kemer–Kumluca region

[29; 5]. In comparable ophiolitic and arid mineral-exploration settings, several authors have shown that multi-temporal optical datasets can be reliably integrated when surface exposure is stable and anthropogenic disturbance is limited [42; 6; 14]. Localized anthropogenic modifications visible between the two dates (quarry expansion, minor road development) were digitized and found to fall outside the ophiolitic outcrops used for training and validation; pixels within these zones were excluded from both sample pools as a precaution. Figure 4 illustrates true-color composites (ASTER and Landsat-9 OLI bands 4-3-2) for visual reference.

Table 1 Specifications of satellite datasets used in this study.

Sensor	Spectral Range Used	Bands	Spatial Resolution	Product Level
ASTER	VNIR + SWIR	Bands 1–9 (VNIR: 1–3; SWIR: 4–9)	15 m (VNIR), 30 m (SWIR)	Level-1T
Landsat-9 OLI	VNIR + SWIR	Bands 2–7 (VNIR: 2–5; SWIR: 6–7)	30 m	Level-1

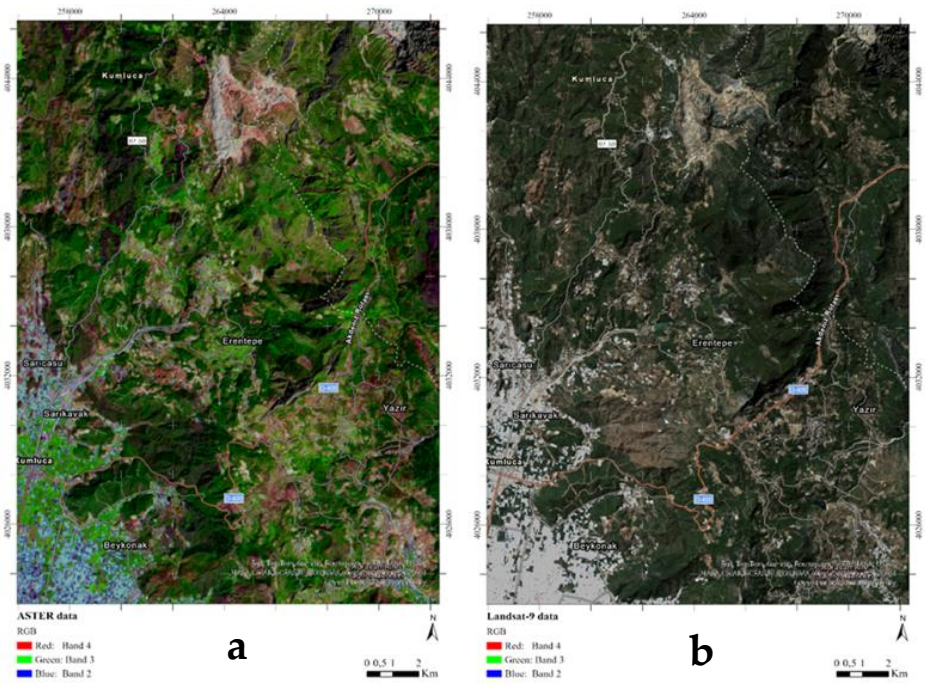


Fig. 4 True-color composites of the study area derived from a) ASTER and b) Landsat-9 OLI imagery using the 4-3-2 band combination.

3.2. Field Sampling and Geochemical Analysis

A detailed description of the geological context of the Tekirova ophiolite and its lithological subdivisions is provided in Section 2 (Geological Setting). Fifty rock samples were collected from ophiolitic units across the Tekirova, Kemer, and Kumluca regions using

stratified sampling based on preliminary field observations and existing geological maps (Fig. 3). Locations were recorded with high-precision GPS. After quality control, 23 fresh, unweathered samples were selected for analysis; the remaining 27 showed significant weathering/alteration and were excluded to avoid bias.

Samples were crushed, pulverized to <63 μm, and rinsed with distilled water to remove adhering dust and soluble salts from arid-field storage, following established protocols for ultramafic rocks in arid environments [6; 42]. Samples were then oven-dried at 60°C prior to analysis. Potential limitations of this protocol are discussed in Section 5.3.

Whole-rock major and trace element compositions, including Cr_2O_3, were determined by X-ray fluorescence (XRF) at the Akdeniz University Engineering Geology Laboratory using a PANalytical Axios spectrometer. Precision was better than 5% for major oxides and 8% for trace elements (based on replicate analyses and international standards such as UB-N and BE-N). Detection limits for Cr_2O_3 were ~10 ppm.

3.3. Image Processing Techniques

3.3.1. Band-Ratio Composites

Band-ratio techniques enhanced lithological contrasts by suppressing topographic effects and emphasizing diagnostic absorption features (Table 2). Each combination was selected based on mineralogical rationale:

- Landsat-9: 6/4, 6/2, 7/6 targets Fe^{2+}/Fe^{3+} variations and ferric oxides in ultramafic rocks [this study].
- Landsat-9: 7/6, 6/5, 4/2 highlights OH-bearing minerals (chlorite, serpentine) via Al–OH and Mg–OH features (Unal et al. 2018).
- Landsat-9: 6/7, 6/2, 6/5 × 5/4 emphasizes serpentine/chlorite signatures (Rajendran et al. 2012).
- ASTER: 5/8, 4/2, 5/4 (novel) — designed to target Mg-OH absorption in serpentine and chlorite (ASTER B8, 2.33 μm) [27; 42], Al-OH absorption in altered mafic units (ASTER B2, 0.66 μm — to be cross-checked with ASTER B4, 1.65 μm), and Fe^{2+} electronic absorption in unaltered olivine/pyroxene captured indirectly via the band-5/band-4 contrast (VNIR–SWIR transition), effectively discriminating serpentinized dunites/harzburgites from mafic/sedimentary units.

Table 2 Band-ratio combinations applied to ASTER and Landsat-9 OLI data.

Sensor	Band-Ratio Combination (R/G/B)	Reference / Rationale
Landsat-9 OLI	6/4, 6/2, 7/6	This study (highlights Fe^{2+}/Fe^{3+} variations)
Landsat-9 OLI	7/6, 6/5, 4/2	enhances OH-bearing minerals (Unal et al. 2018)
Landsat-9 OLI	6/7, 6/2, 6/5 × 5/4	serpentine/chlorite mapping (Rajendran et al. 2012)
ASTER	5/8, 4/2, 5/4	This study targets Mg-OH absorption in serpentine/chlorite and Al-OH alteration

These are shown in Figure 5 for comparison.

233 3.3.2. Principal Component Analysis (PCA) and Minimum Noise Fraction (MNF)

234 PCA and MNF reduced dimensionality and enhanced subtle variations in VNIR-
235 SWIR bands. RGB composites of PC1–PC3 and MNF2–MNF4 were generated for visual
236 interpretation (Figs. 6 and 7).
237
238
239 3.3.3. Decorrelation Stretch

240 Decorrelation stretching maximized color separation in selected triplets (ASTER
241 bands 7-6-5; Landsat-9 bands 7-5-2) (Gillespie et al. 1986), improving boundary discrimi-
242 nation (Fig. 9).
243

244 *3.4. Supervised Classification Using Support Vector Machine (SVM)*

245 SVM classification with radial basis function (RBF) kernel was implemented in ENVI
246 5.3 to produce the final lithological map. SVM separates classes by finding an optimal
247 hyperplane in high-dimensional space, suitable for non-linear spectral boundaries in lith-
248 ological data.
249 **Input features (stacked for SVM):** All original bands. A detailed input stack is pro-
250 vided in Table 3.
251 **Training and validation:** 150 ground truth points (from field mapping) trained five
252 classes (Tahtali Nappe, Ophiolite, Alakircay Nappe, Kirderek Formation, Quaternary). An
253 independent validation set of 69 points (stratified random sampling in ArcGIS Pro) as-
254 sessed accuracy. Hyperparameters were optimized via 5-fold cross-validation (gamma =
255 0.01, C = 100, yielding 88.5% cross-validation accuracy). The confusion matrix (Table 4)
256 shows overall accuracy of 90% (Kappa = 0.87), with class-specific producer's and user's
257 accuracies indicating robust performance, particularly for ophiolite (user's accuracy 81%)
258 and Quaternary (100%). Minor confusion occurred between adjacent nappe units due to
259 spectral similarity [40; 45].
260 The resulting map (Fig. 9) integrates these results for spatial analysis with geochem-
261 ical data.

262 ## 4. Results

263 The integrated application of spectral enhancement techniques and supervised clas-
264 sification to ASTER and Landsat-9 OLI data produced detailed maps of the ophiolitic li-
265 thologies in the Tekirova-Kemer-Kumluca region. The results are presented following the
266 methodological workflow, from spectral enhancement to final classification and geochem-
267 ical validation.
268
269 *4.1. Spectral Characterization and Mineralogical Baseline*
270 Before evaluating the image enhancement results, it is essential to establish the spec-
271 tral behavior of the target lithologies in the study area. The discrimination of ophiolitic
272 units relies on identifying specific absorption features in the electromagnetic spectrum.
273 Table 3 summarizes the diagnostic reflectance values and absorption pits of key minerals
274 such as olivine, enstatite, and serpentine, which dictate the spectral response in the VNIR
275 and SWIR regions. These physical properties provide theoretical justification for the band
276 selection and ratios used in this study, particularly highlighting the high-reflectance plat-
277 eaus and deep absorption centers (e.g., the Mg-OH feature at 2.32 μm).
278
279
280 Table 3 Diagnostic spectral reflectance values for the primary ophiolitic minerals

Wavelength (μm)	ASTER band	Landsat-9 band	Olivine (Refl.)	Serpentine (Refl.)	Enstatite (Refl.)	Notes / Absorption feature
0.45	—	B2 (0.48)	0.08	0.15	0.12	Visible (Blue) baseline
0.70	B2 (0.66)	B4 (0.65)	0.25	0.40	0.35	Visible (Red) Fe^{3+} shoulder
0.90	B3 (0.81)	B5 (0.86)	0.12 ★	0.45	0.18 ★	Fe^{2+} VNIR absorption (olivine, pyroxene)
1.05	—	—	0.05 ★	0.48	0.30	Olivine maximum Fe^{2+} absorption
1.60	B4 (1.66)	B6 (1.61)	0.40	0.55	0.50	SWIR Al-OH baseline
2.10	B5 (2.17)	B7 (2.20)	0.45	0.52	0.48	Al-OH absorption region
2.32	B8 (2.34)	(within B7)	0.42	0.12 ★	0.40	Mg-OH absorption (ASTER B8) diagnostic of serpentine
2.50	—	—	0.38	0.30	0.35	SWIR terminal reflectance

★ = Absorption minimum (spectral dip)

4.2. Spectral Enhancement and Band Ratio Results

Band ratio composites effectively highlighted spectral contrasts between major rock units. For Landsat-9 OLI, the RGB composite of bands (6/4, 6/2, 7/6) delineated ophiolitic serpentinites and dunites in distinctive magenta and pink hues, while carbonate-dominated units appeared in cyan and blue (Fig. 5a). The composite (7/6, 6/5, 4/2) further enhanced the contrast of altered ferromagnesian minerals, showing ophiolitic rocks in green to yellow colors (Fig. 5b). The selection of band ratios was based on specific mineralogical absorption features: (a) The 6/4, 6/2, 7/6 composite highlights variations in Fe^{2+}/Fe^{3+} ratios and ferric iron oxides; (b) the 7/6, 6/5, 4/2 composite (after Sultan et al. 1986) enhances the contrast of hydroxyl-bearing alteration minerals such as chlorite and serpentine; (c) the 6/7, 6/2, 6/5 × 5/4 composite (after Mars and Rowan 2006) targets serpentine and chlorite signatures; and (d) the novel 5/8, 4/2, 5/4 composite leverages strong Mg-OH absorption in ASTER band 8 (2.33 μm) characteristic of serpentine and chlorite, with the band-4 (1.65 μm) reflectance baseline contributing the Al-OH contrast for altered mafic rocks.

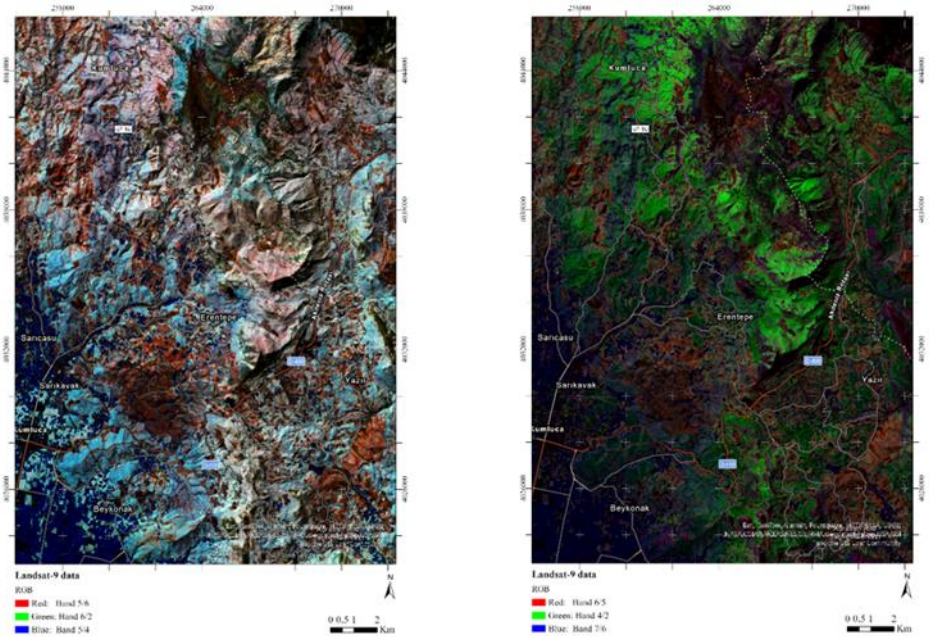
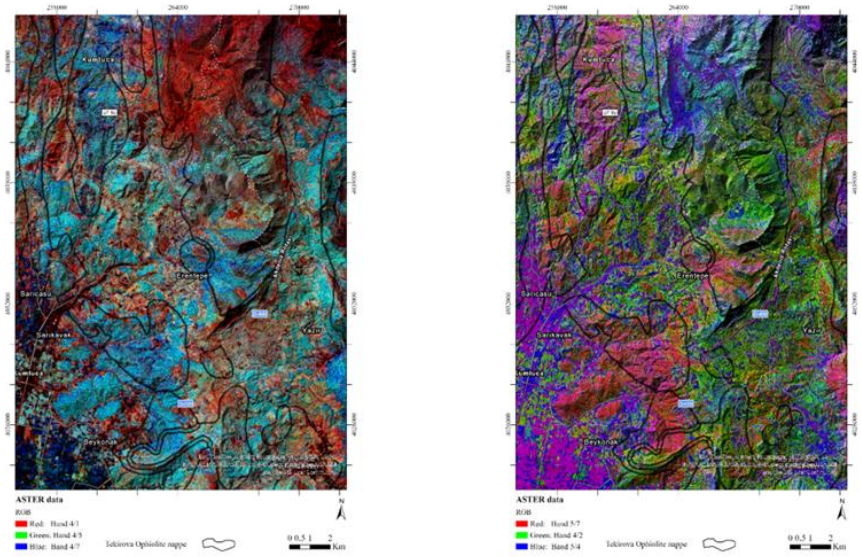


Fig. 5 Landsat-9 OLI RGB band-ratio composites of the study area: (a) 6/4, 6/2, 7/6; (b) 6/5, 4/2 , 7/6 (after Sultan et al. 1986) Band ratios are assigned to red, green, and blue channels, respectively (Rowan et al. 2005).

For ASTER data, the novel band ratio composite (5/8, 4/2, 5/4) in RGB provided the most effective discrimination for this specific region. In this composite (Fig. 6b), highly serpentinized ultramafic rocks (dunite, harzburgite) and mafic cumulates (gabbro) were displayed in bright magenta and green tones, respectively. This is attributed to the strong Mg-OH absorption in ASTER band 8 (2.33 μm) characteristic of serpentine and chlorite [27; 42], and the reflectance contrast at ASTER band 4 (1.65 μm) associated with Al-OH absorption in altered mafic rocks.



(a) (b)

Fig. 6 ASTER RGB band ratio images: (a) 4/1, 4/5, 4/7 (after 42); (b) 5/8, 4/2, 5/4 (this study).

Principal Component Analysis (PCA) and Minimum Noise Fraction (MNF) transformations concentrated spectral information and improved signal-to-noise ratios. The RGB composite of PC1, PC2, and PC3 for ASTER data (Fig. 7a) showed ophiolitic units in dark blue and green, sharply contrasting with the red and orange tones of sedimentary rocks. The corresponding Landsat-9 PCA composite (Fig. 7b) showed similar lithological contrasts at lower mineralogical specificity. The MNF composites (Fig. 8a–b) provided enhanced intra-ophiolite discrimination, with serpentinized ultramafic rocks rendered in red/yellow and gabbroic bodies in green/blue.

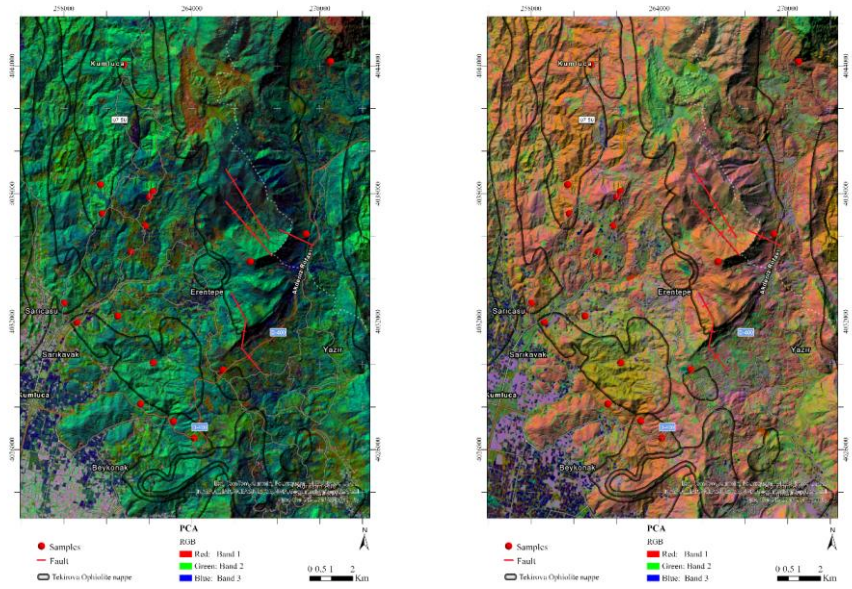


Fig. 7 RGB composites of dimensionality-reduction transforms applied to the ASTER and Landsat-9 OLI datasets: (a) PC1-PC2-PC3 from ASTER; (b) PC1-PC2-PC3 from Landsat-9 OLI.

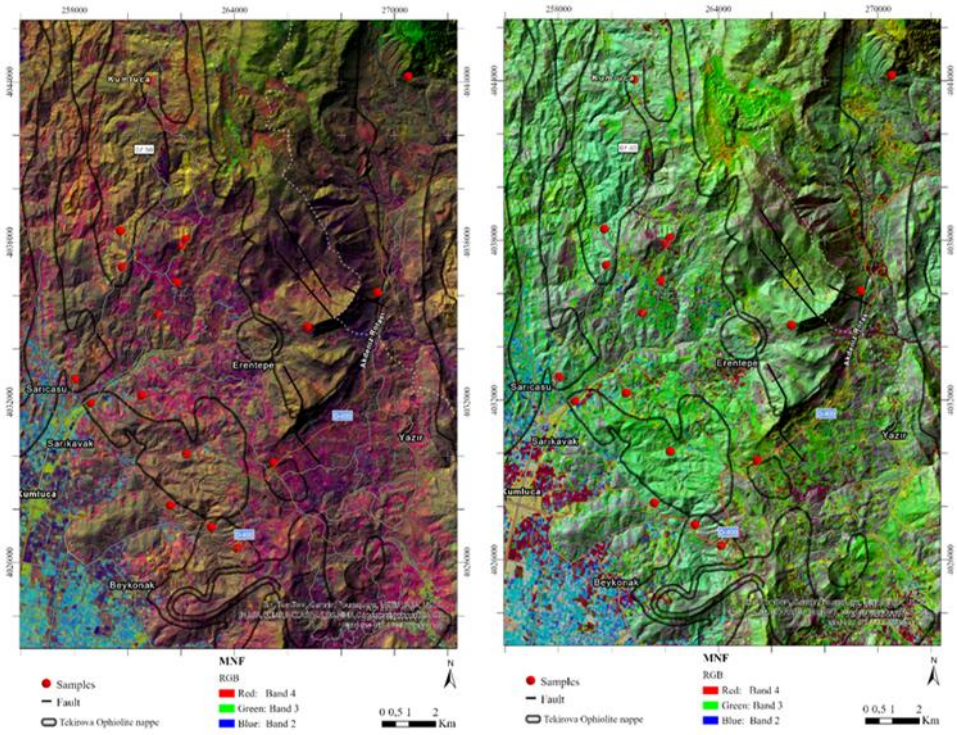


Fig. 8 Minimum Noise Fraction (MNF) RGB composites: **(a)** MNF4, MNF3, MNF2 for ASTER; **(b)** MNF4, MNF3, MNF2 for Landsat-9 OLI, showing lithological units in the study area.

4.3. Decorrelation Stretch Results

Three-band color composites of the ASTER and Landsat-9 OLI imagery were selected to perform the decorrelation stretch. Bands 7, 6, and 5 were used for ASTER, and bands 7, 5, and 2 for Landsat-9 OLI, based on the spectral characteristics of the rock units in the study area. ASTER band 2 (red) and Landsat-9 band 5 (NIR) carry information related to iron-bearing minerals; ASTER band 5 corresponds to Landsat-9 band 7 and provides information on hydroxyl-bearing minerals; ASTER band 8 captures absorption features diagnostic of carbonate and serpentine minerals (Pour et all. 2018). The resulting decorrelated image discriminates most of the ophiolite rock types into distinct color domains, in agreement with the regional geological map (Fig. 9)

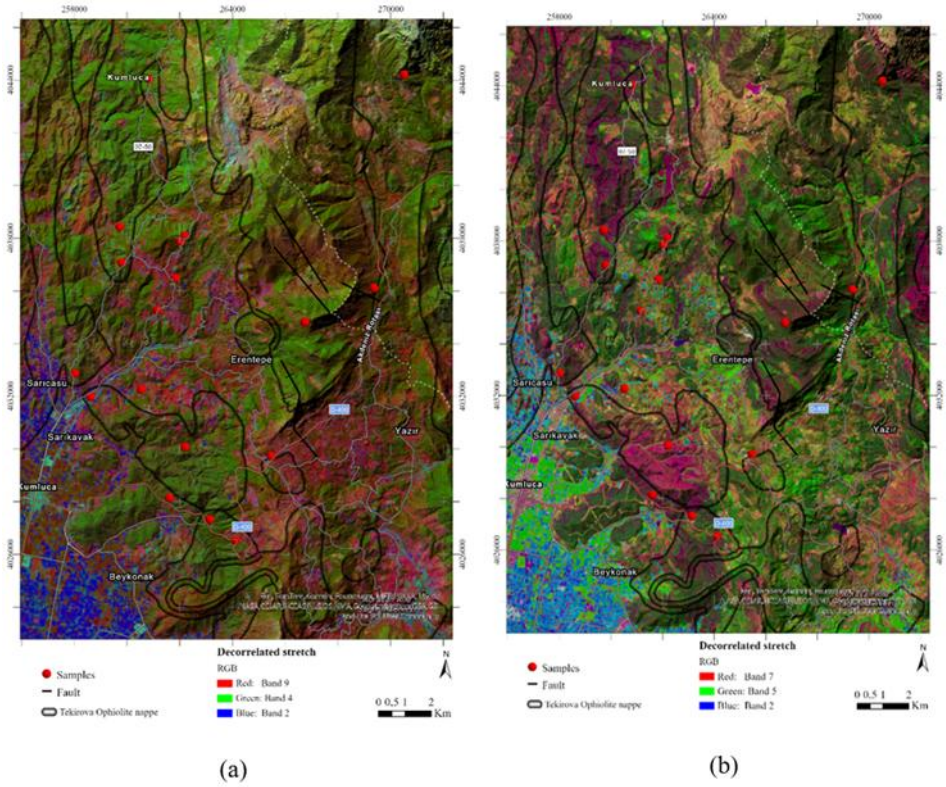


Fig. 9 Decorrelation-stretch RGB composites: (a) ASTER bands 7-6-5; (b) Landsat-9 OLI bands 7-5-2, enhancing boundary discrimination between lithological units in the study area.

4.4. Lithological Classification Using Support Vector Machine (SVM)

The supervised SVM classification (Mountrakis et al. 2011) synthesized spectral information from all enhancement techniques to produce a comprehensive lithological map (Fig. 10). The classifier effectively distinguished five key units: Tahtali Nappe, Ophiolite (ultramafic/mafic complex), Alakircay Nappe, Kirderek Formation, and Quaternary deposits.

Accuracy assessment using an independent validation dataset (n=69 points) yielded an Overall Accuracy of 90% and a Kappa Coefficient of 0.87 (Table 4), indicating very high agreement with reference data. The Quaternary class showed high classification reliability (User's Accuracy: 100%, n = 19; 95% Wilson CI = 83.2%–100%). The Kirderek Formation class showed no misclassifications within its very small validation sample (n = 2; 95% Wilson CI = 34.2%–100%); however, given the limited statistical power, this result should be interpreted with caution and not as a robust class-level validation (Foody 2020). The

spectrally heterogeneous "Ophiolite" class showed robust accuracy (User's Accuracy: 81%, n = 16; 95% Wilson CI = 57.0%–93.4%), with minor confusion primarily with the adjacent Tahtali Nappe (Wilson 1927).

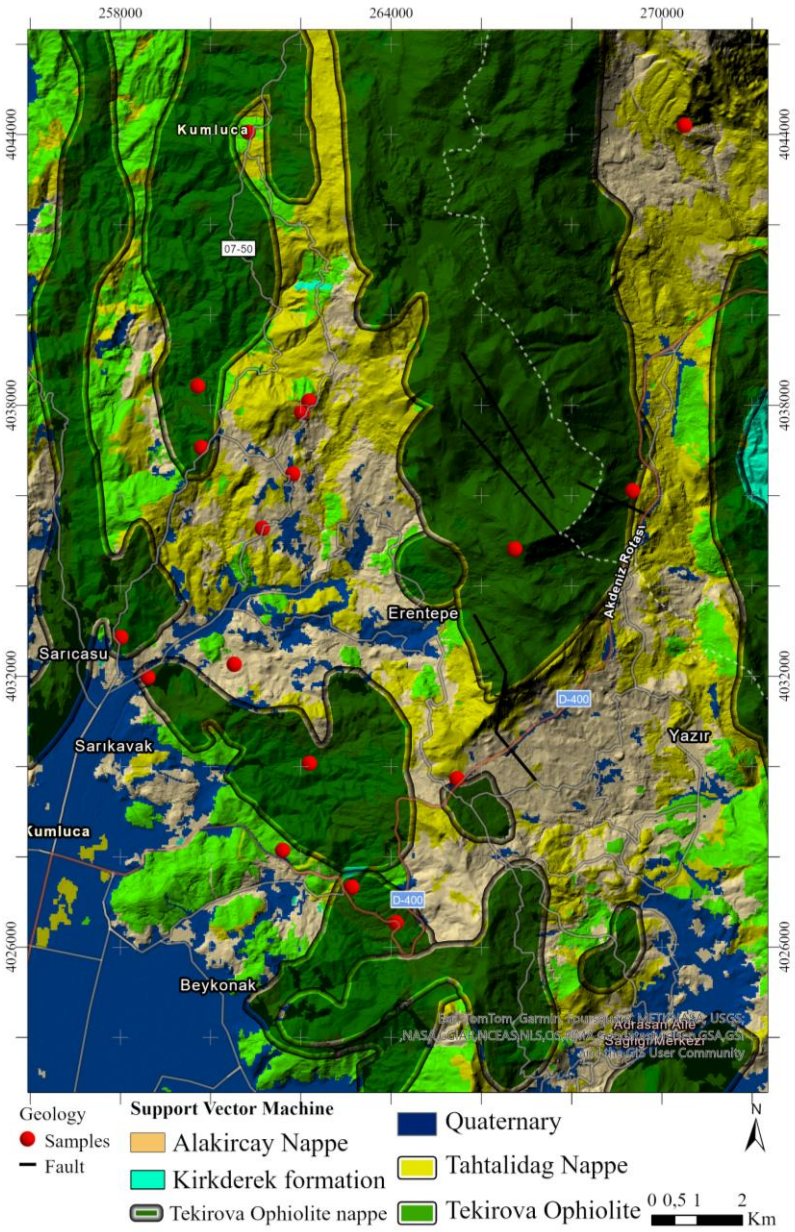


Fig. 10 Supervised classification image-map of the study area.

4.4.1. Classifier benchmark

To justify the selection of SVM, a Maximum Likelihood (ML) classifier was trained on the same fused input stack (original bands + band ratios + PCA/MNF components) and evaluated on the same independent validation set (n = 69) (Maxwell et al. 2018). The ML classifier achieved an overall accuracy of 78.3% (κ = 0.71; MCC = 0.68), substantially below the SVM performance (OA = 90%, κ = 0.87, MCC = 0.85). This 11.7-percentage-point gap in overall accuracy is consistent with previously reported margins between SVM and ML in small-sample, high-dimensional lithological classification settings [43; 44]. A more comprehensive benchmark including Random Forest, Gradient Boosting, and deep-learning

approaches falls outside the scope of this study, but is identified as an important direction for future methodological work in this region

Table 4. Confusion matrix and accuracy assessment for the SVM classification on the independent validation set (n = 69). Reported metrics include Overall Accuracy (90%), Kappa coefficient (κ = 0.87), and Matthews Correlation Coefficient (MCC = 0.85), with class-specific Producer's and User's Accuracies and 95% Wilson confidence intervals. *Note: the perfect classification of the Kirderek Formation (n = 2) reflects the very limited surface exposure of this unit and should be interpreted as the absence of misclassification within a small sample (95% Wilson CI = 34.2%–100%), not as a robust validation of class-level performance*

Reference → Classified ↓	Tahtali Nappe	Ophiolite	Alakircay Nappe	Kirderek Frm.	Quaternary	Total	Prod. Acc. (%)	95% CI (Wilson)
Tahtali Nappe	15	3	1	0	0	19	79	56.7%–91.5%
Ophiolite	1	13	1	0	0	15	87	62.1%–96.3%
Alakircay Nappe	1	0	13	0	0	14	93	68.5%–98.7%
Kirderek Formation	0	0	0	2	0	2	100	34.2%–100%
Quaternary	0	0	0	0	19	19	100	83.2%–100%
Total	17	16	15	2	19	69	—	—
User Acc. (%)	88	81	87	100	100	—	—	—
User Acc. 95% CI (Wilson)	65.7%–96.7%	57.0%–93.4%	62.1%–96.3%	34.2%–100%	83.2%–100%	—	—	—

Overall Accuracy = 90%
Kappa Coefficient (κ) = 0.87
Matthews Correlation Coefficient (MCC) = 0.85

4.5. Integration with Geochemical Data and Chromium Distribution

Geochemical analysis of 23 fresh samples from the ophiolitic units revealed Cr_2O_3 concentrations ranging from 100 to 6900 ppm (mean: 2548 ppm). Table 5 summarizes the chromium distribution according to the primary lithological classes identified in the field.

Table 5 Summary statistics of Cr_2O_3 concentrations (ppm) by lithological unit (SD = standard deviation; CV = coefficient of variation).

Lithology	n	Min (ppm)	Max (ppm)	Mean± SD (ppm)	Median (ppm)	CV(%)
Serpentinite/ Dunite	**14**	**1200**	**6900**	**3850 ± 1425**	**3660**	**37.0**
Gabbro/ Mafic rocks	**6**	**100**	**850**	**420 ± 188**	**400**	**44.6**
Mixed/ Sedimentary	**3**	**150**	**500**	**280 ± 88**	**266**	**31.2**

5. Discussion

The spectral classifications obtained in our study have once again highlighted the need for 'correlating remote sensing data with quantitative geochemical data,' which is frequently emphasized in the literature. Although chromite prospectivity is well-defined in the literature, the process of directly verifying the classified ultramafic areas with geochemical analyses is still limited. For example, the detailed petrological and geochemical data presented in the Lycian ophiolites constitute a critical reference for supporting 'permissive lithological zones' determined by remote sensing with physical evidence (Robertson and Woodcock 1980). Approaches such as the advanced integration of applied magnetic and remote sensing data should become standard in the future to address such geochemical deficiencies and increase mapping accuracy (Güneş 2018)

5.1. Implications for Ophiolite Mapping

The results demonstrate that integrating ASTER and Landsat-9 OLI data improves lithological discrimination within complex ophiolitic terrains relative to single-sensor approaches. ASTER SWIR bands enhance sensitivity to mineralogical variations associated with ultramafic rocks, particularly serpentinization and Fe-bearing silicates, whereas Landsat-9 OLI contributes improved radiometric performance and spatial consistency at the regional scale. The SVM-based classification effectively integrates these complementary datasets to delineate ophiolitic units with a level of detail exceeding that of existing regional geological maps (Figs. 7 and 9).

The exploratory use of PCA and MNF highlights internal heterogeneity within ultramafic units and assists in identifying spectral patterns relevant to ophiolite mapping. However, consistent with state-of-the-art practice, the final lithological interpretation is best supported by supervised classification results constrained by geological knowledge and field-based validation. This approach addresses the limitations noted by previous studies that relied heavily on qualitative image interpretation without robust validation.

5.2. Chromium Prospectivity and Geological Constraints

Chromium mineralization in ophiolitic settings is controlled primarily by lithological and structural factors, with podiform chromite bodies preferentially hosted within dunite lenses and zones of intense serpentinization. It is crucial to clarify that the remote sensing results presented here do not constitute direct detection of chromite deposits. Rather, they define lithological domains (serpentinized dunites and harzburgites) that are geologically favorable for hosting podiform chromite mineralization at a regional scale (fig.11).

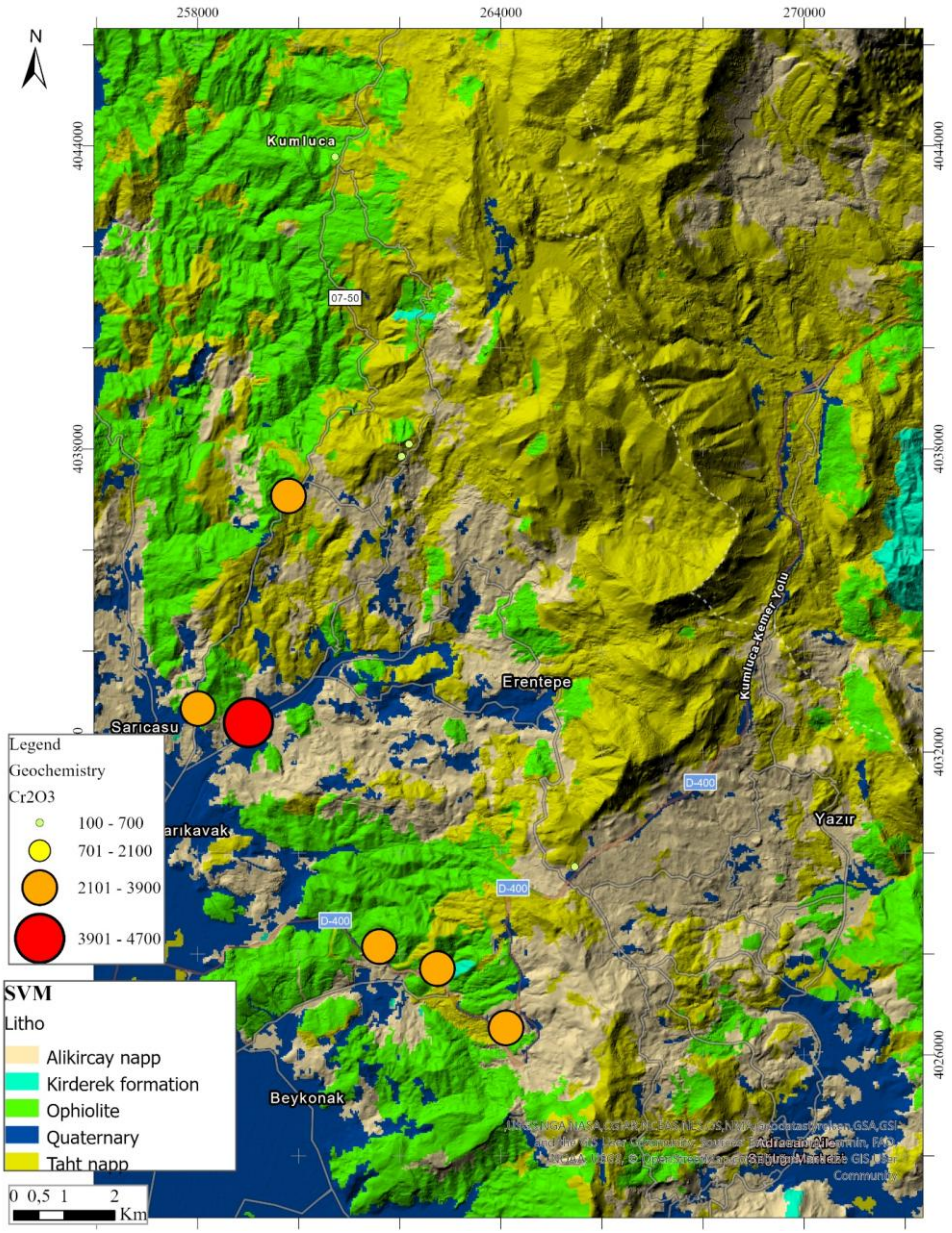


Fig. 11 Spatial distribution of Cr_2O_3 sample concentrations (n = 23) overlaid on the SVM-classified lithological map of the Tekirova–Kumluca region. Sample points are symbolized by proportional circles scaled to Cr_2O_3 content (ppm). Background lithology classes are as in Figure 9. Topographic shading derived from the 30-m SRTM DEM.

The chromite prospectivity assessment is considered preliminary due to the limited availability of subsurface data and the reconnaissance-scale nature of field sampling; however, the spatial coherence between mapped ultramafic units, alteration signatures, and known chromite occurrences supports the robustness of the remote sensing-based predictions. The limited number of geochemical samples and the spatial resolution of the satellite data constrain the level of confidence that can be assigned to prospectivity predictions. Consequently, the results should be viewed as a first-order screening tool to guide more detailed field investigations and targeted geochemical sampling.

To further elucidate the geochemical relationships controlling chromium enrichment, a Pearson correlation analysis was performed on major oxide compositions from the 23 ophiolite samples (Fig. 12). The correlation matrix reveals a strong positive

correlation between Cr_2O_3 and MgO (r = 0.92, p<0.001), which is consistent with chromite occurrence within magnesian-rich ultramafic host rocks, specifically dunites and serpentinized harzburgites. Conversely, significant negative correlations were observed between Cr_2O_3 and both Al_2O_3 (r = -0.81, p<0.01) and SiO_2 (r = -0.62, p<0.01), reflecting the depletion of these oxides in chromite-bearing ultramafic lithologies relative to mafic cumulates. This geochemical signature aligns with the established petrogenesis of podiform chromitites formed during partial melting and melt-rock interaction in the mantle wedge of supra-subduction zone settings. These correlations, observed in the analyzed sample (n = 23), are consistent with the established petrogenetic controls on chromium enrichment in supra-subduction zone ophiolites and lend support to the lithological identity of the SVM-classified ultramafic domains. We note that this geochemical pattern confirms the lithological identity of the classified pixels rather than independently validating the spatial accuracy of the classification, which is assessed by the independent 69-point validation set (Table 4).

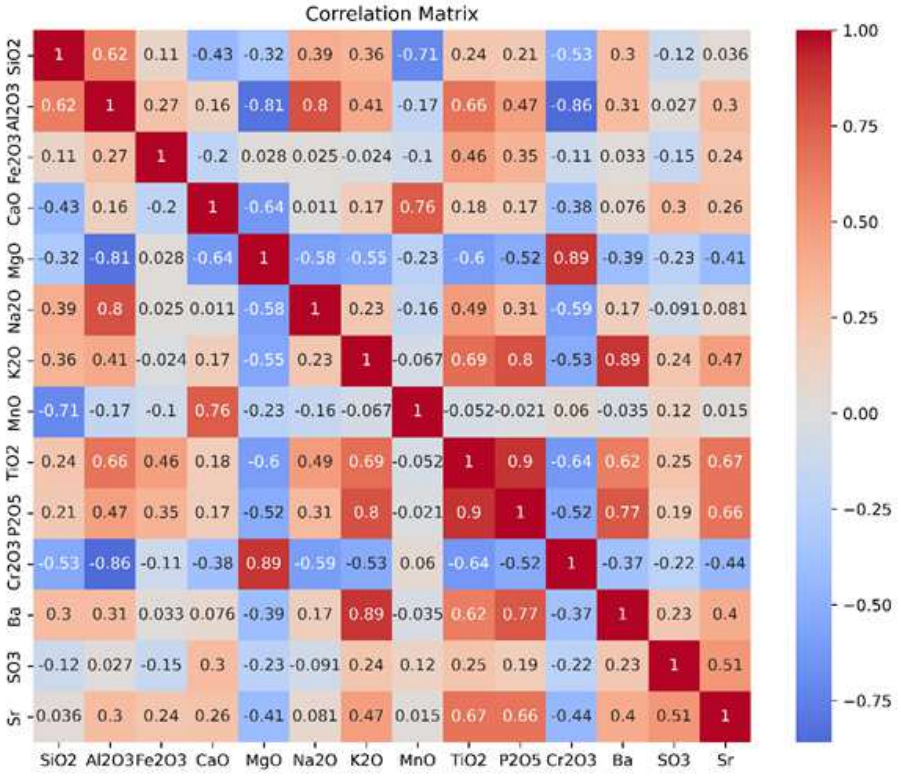


Fig. 12 Pearson correlation matrix of selected major oxides from ophiolite samples (n=23). Correlation coefficients significant at (p<0.05), (p<0.01), and (p<0.001) levels are indicated. The strong positive Cr_2O_3-MgO correlation (r=0.92***) and negative Cr_2O_3-SiO_2 (r=-0.62**) and Cr_2O_3-Al_2O_3 (r=-0.81**) correlations are consistent with chromite enrichment in magnesian-rich dunitic host rocks. Color scale ranges from dark blue (r=-1, strong negative correlation) through white (r=0, no correlation) to dark red (r=+1, strong positive correlation).

5.3 Methodological Limitations and Transferability

Several limitations inherent to multispectral remote sensing must be acknowledged. A first limitation concerns the 16-year temporal gap between the ASTER (2006) and Landsat-9 OLI (2022) acquisitions. Although the qualitative stability assessment reported in Section 3.1 indicates that vegetation cover and surface exposure are essentially stable across the ophiolitic outcrops, residual uncertainty cannot be excluded for areas affected

by minor anthropogenic disturbance or progressive weathering. The two sensors are therefore used as complementary spectral layers (multi-sensor integration) rather than as a strictly contemporaneous pixel-level fusion, an approach consistent with recent multi-temporal multispectral studies of mineral exploration [42; 12].The spatial resolution of both ASTER and Landsat-9 OLI restricts the detection of small chromite bodies, which commonly occur at scales below individual pixel sizes. Additionally, surface weathering, vegetation cover, and topographic effects may obscure or modify spectral signatures in certain areas. Furthermore, the sample washing step, while necessary to remove adhering dust and soluble salts in this arid environment, warrants caution in similar studies. Although the protocol minimizes surface contamination without substantially altering bulk geochemistry (Bilgilioğlu 2024), the potential loss of fine-grained fractions, particularly soft serpentine particles, which can be physically dislodged during rinsing—cannot be entirely excluded if centrifugation is not applied. This limitation may affect the representativeness of fine-fraction geochemistry, especially for highly altered serpentinized samples (Hanghøj et al. 2010). Future studies should consider paired washed/unwashed analyses, or alternative protocols such as ultrasonic cleaning or freeze-drying (Velbel 2009), to quantify and mitigate this potential bias.

Despite these limitations, the workflow presented here is transferable to other ophiolitic regions with similar geological characteristics. The emphasis on transparent methodology, supervised classification with independent validation, and integration with geochemical constraints enhances reproducibility and supports application beyond the study area. Future work could incorporate higher-resolution hyperspectral data or unmanned aerial vehicle (UAV) imagery to improve detection of small-scale mineralization features.

5.4 Field Verification

Field observations were conducted to validate the remote sensing classification results and investigate the contact relationships between the ophiolitic units. As shown in Figure 13, the serpentinized harzburgites in the Tekirova and Kemer zones exhibit characteristic shear zones and intense foliation, distinguishing them from the massive dunitic cores. These field exposures confirm the high accuracy of the ASTER Band Ratio (5/8, 4/2, 5/4) composite in delineating the alteration surfaces of ultramafic rocks.



Kumluca, Sample 9; (36.45867°N/30.34609°E)



Kumluca, Sample 11; (36.45646°N/ 30.34457°E)



Fig. 13 Field photographs of the Tekirova, Kemer, and Kumluca ophiolite zones illustrating the structural deformation and surface alteration of serpentinized peridotites.

5.5. Study Limitations

Despite the effectiveness of the integrated mapping approach, this study encounters certain statistical constraints that warrant discussion. To maintain a high standard of spectral validation, the initial sample pool of 50 was refined to 23 specimens, specifically excluding those with significant surface weathering or oxidative crusts that could skew reflectance data. While this prioritization of 'fresh' samples ensures spectral purity, it naturally limits the statistical breadth of the dataset. Caution should be applied to the 'Mixed/Sedimentary' class where the small subset ($n=3$) restricts the generalizability of its classification accuracy. Future research efforts should aim to expand the spatial density of field-verified points to further validate the predictive robustness of these remote sensing models across more diverse lithological exposures.

The literature has reinforced the importance of multi-sensor and SVM-based mapping approaches (Badr et al. 2026b; Eskandari et al. 2023). It has also been noted that this approach will address a significant weakness in literature by storing remote sensing models with quantitative geochemical data (Pearson analysis) according to petrological laws (Çelik and Chiaradia 2008). The data obtained in this study confirm the effectiveness of modern remote sensing techniques in mapping ophiolitic complexes and show strong parallelism with the fundamental methodological approaches in literature. In another study, the integration of Landsat-9 OLI and ASTER data achieved success for single-sensor approaches by combining Landsat-9's superior radiometric performance with ASTER's mineralogical sensitivity (Carvalho et al. 2025). However, according to a different study on Egyptian ophiolites, it revealed the necessity of "multi-sensor integration" and the high

accuracy of SVM-based mapping approaches [14, 15]. This multi-sensor integration method has been successfully applied in the Tekirova-Kumluca region and closes a significant gap in the literature by validating remote sensing models with quantitative geochemical data (Pearson analysis). Furthermore, in terms of methodology, the SVM (Support Vector Machines) based classification we used is also supported in this study. Spectral classifications were numerically validated with a strong Pearson correlation between Cr_2O_3 and MgO ($r = 0.92$, $p < 0.001$). In such studies, the need for new data based on high-resolution data from UAVs has been addressed (Eskandari et al. 2023). In particular, the importance of a multi-scale mapping strategy has been further confirmed, and it has been stated that integrated models supported by magnetic and geochemical data maximize the accuracy of mineral exploration (Eldosouky et al. 2024). Our findings are also important in demonstrating the success of satellite-based models as a "first-order scanning tool" on a regional scale.

6. Conclusions

This study demonstrates that the integrated use of ASTER and Landsat-9 OLI multispectral data provides an effective and transferable framework for detailed lithological mapping in structurally complex ophiolitic terrains. The synergistic combination of the two datasets enhanced the discrimination of ultramafic and mafic units beyond the capability of single-sensor approaches by leveraging ASTER's sensitivity in the SWIR mineralogical bands and Landsat-9's superior radiometric consistency.

The SVM-based supervised classification yielded a robust lithological map with an overall accuracy of 90% (Kappa = 0.87; Matthews Correlation Coefficient = 0.85), validated against an independent set of 69 stratified random points, offering a reliable and updated spatial framework for regional geological interpretation. The strong spatial correspondence between elevated Cr_2O_3 geochemical concentrations, characterized by a strong Cr_2O_3-MgO correlation and the spectrally distinct ultramafic units classified by SVM is consistent with the remote sensing methodology. While the spatial resolution of the sensors precludes the direct detection of small-scale chromite pods, the results successfully delineate lithological domains that are geologically permissive for hosting this style of mineralization.

In summary, the proposed multi-sensor remote sensing workflow, underpinned by field validation and geochemical analysis, represents a reproducible and efficient methodology for regional-scale ophiolite mapping and preliminary mineral prospectivity assessment. This integrated approach can significantly contribute to optimizing exploration strategies in similar ophiolitic belts worldwide by bridging the gap between regional-scale remote sensing and ground-truth data, serving as a cost-effective first-pass screening tool.

Abbreviations

ASTER: Advanced Spaceborne Thermal Emission and Reflection Radiometer

OLI: Operational Land Imager

SVM: Support Vector Machine

PCA: Principal Component Analysis

MNF: Minimum Noise Fraction

SWIR: Short-Wave Infrared

VNIR: Visible and Near-Infrared

Declarations

Funding This research was financially supported by the Scientific Research Projects Coordination Unit of Akdeniz University (Project Number FYL2016-1038).

Competing interests The authors declare that they have no known competing financial interests or personal relationships that could have appeared to influence the work reported in this paper.

Ethics approval Not applicable.

Consent to participate Not applicable.

Consent for publication Not applicable.

Data availability The ASTER and Landsat-9 OLI datasets analysed in this study are openly available from the United States Geological Survey (USGS) EarthExplorer portal (https://earthexplorer.usgs.gov). The geochemical and field datasets generated and analysed during the current study are available from the corresponding author on reasonable request.

Author contributions [To be completed by all authors prior to submission. Suggested CRediT roles to assign: Conceptualization; Methodology; Software; Validation; Formal analysis; Investigation (field sampling and petrography); Resources; Data curation; Writing – original draft; Writing – review and editing; Visualization; Supervision; Funding acquisition.]

Acknowledgments Cartographic visualizations were prepared using Esri basemap imagery. The authors gratefully acknowledge insightful field discussions with colleagues.

References

Abrams M, Yamaguchi Y (2019) Twenty years of ASTER contributions to lithologic mapping and mineral exploration. Remote Sens 11:1394. https://doi.org/10.3390/rs11111394

Amer R, Kusky T, Ghulam A (2010) Lithological mapping in the central Eastern Desert of Egypt using ASTER data. J Afr Earth Sci 56:75-82. https://doi.org/10.1016/j.jafrearsci.2009.06.004

Arai S, Yurimoto H (1994) Podiform chromitites of the Tari-Misaka ultramafic complex, southwestern Japan, as mantle-melt interaction products. Econ Geol 89(6):1279-1288. https://doi.org/10.2113/gsecongeo.89.6.1279

Badr MM, El Mezayen AM, Azab AE et al (2026) Integrated multispectral remote sensing and field investigations for delineating ophiolitic complexes of Wadi Ghadir, southeastern desert, Egypt. Sci Rep 16:798. https://doi.org/10.1038/s41598-025-32272-8

Badr MM, El Mezayen AM, El Azab A et al (2026) Mapping Gabel Lawi ophiolitic melange and associated rocks in the South Eastern Desert, Egypt. Mediterr Geosci Rev 8:71-91. https://doi.org/10.1007/s42990-026-00221-w

Bağcı U (2004) Geochemistry and petrology of the Kızıldağ (Hatay) and Tekirova (Antalya) ophiolites. Dissertation, Çukurova University (in Turkish with English abstract)

Bağcı U, Parlak O (2009) Petrology of the Tekirova (Antalya) ophiolite (southern Turkey): evidence for diverse magma generations and their tectonic implications during Neotethyan subduction. Int J Earth Sci 98:387-405. https://doi.org/10.1007/s00531-007-0242-7

Bilgilioğlu H (2024) Evaluation of alteration in the geothermal province west of Cappadocia, Türkiye: mineralogical, petrographical, geochemical, and remote sensing data. Open Geosci 16(1):20220675. https://doi.org/10.1515/geo-2022-0675

Carvalho M, Cardoso-Fernandes J, González FJ, Teodoro AC (2025) Comparative performance of Sentinel-2 and Landsat-9 data for raw materials' exploration onshore and in coastal areas. Remote Sens 17(2):305. https://doi.org/10.3390/rs17020305

Çelik ÖF (2007) Metamorphic sole rocks and their mafic dykes in the eastern Tauride Belt ophiolites (southern Turkey): implications for OIB-type magma generation following slab break-off. Geol Mag 144(5):849-866. https://doi.org/10.1017/S0016756807003573

630 Çelik ÖF, Chiaradia M (2008) Geochemical and petrological aspects of dike intrusions in the Lycian ophiolites (SW Turkey): a case
631 study for the dike emplacement along the Tauride Belt ophiolites. Int J Earth Sci 97(6):1151-1164. https://doi.org/10.1007/s00531-
632 007-0204-0
633 Çelik ÖF, Delaloye MF (2003) Origin of metamorphic soles and their post-kinematic mafic dyke swarms in the Antalya and Lycian
634 ophiolites, SW Turkey. Geol J 38(3-4):235-256. https://doi.org/10.1002/gj.954
635 Chavez PS Jr (1988) An improved dark-object subtraction technique for atmospheric scattering correction of multispectral data. Re-
636 mote Sens Environ 24(3):459-479. https://doi.org/10.1016/0034-4257(88)90019-3
637 Chen Y, Wang Y, Zhang F, Dong Y, Song Z, Liu G (2023) Remote sensing for lithology mapping in vegetation-covered regions:
638 methods, challenges, and opportunities. Minerals 13(9):1153. https://doi.org/10.3390/min13091153
639 Dilek Y, Thy P, Hacker B, Grundvig S (1999) Structure and petrology of Tauride ophiolites and mafic dike intrusions (Turkey): im-
640 plications for the Neotethyan Ocean. Geol Soc Am Bull 111(8):1192-1216. https://doi.org/10.1130/0016-7606(1999)111
641 Eldosouky AM, Eleraki M, Mansour A et al (2024) Geological controls of mineralization occurrences in the Egyptian Eastern Desert
642 using advanced integration of remote sensing and magnetic data. Sci Rep 14:16700. https://doi.org/10.1038/s41598-024-66924-y
643 Engin T (1985) Petrology of the peridotite and structural setting of the Batı Kef-Doğu Kef chromite deposits, Guleman, Elazığ, eastern
644 Turkey. In: Metallogeny of basic and ultrabasic rocks. Institution of Mining and Metallurgy, pp 229-240
645 Eskandari A, Hosseini M, Nicotra E (2023) Application of satellite remote sensing, UAV-geological mapping, and machine learning
646 methods in the exploration of podiform chromite deposits. Minerals 13(2):251. https://doi.org/10.3390/min13020251
647 Foody GM (2020) Explaining the unsuitability of the kappa coefficient in the assessment and comparison of the accuracy of thematic
648 maps obtained by image classification. Remote Sens Environ 239:111630. https://doi.org/10.1016/j.rse.2019.111630
649 Gabr S, Ghulam A, Kusky T (2010) Detecting areas of high-potential gold mineralizations using ASTER data. Ore Geol Rev 38:59-69.
650 https://doi.org/10.1016/j.oregeorev.2010.05.007
651 Gad S, Kusky T (2007) ASTER spectral ratioing for lithological mapping in the Arabian-Nubian Shield. Gondwana Res 11(3):326-335.
652 https://doi.org/10.1016/j.gr.2006.02.010
653 Gillespie, A. R., Kahle, A. B., & Walker, R. E. (1986). Color enhancement of highly correlated multispectral images. *Remote Sensing of*
654 *Environment*, 20(3), 209-235.
655 González-Jiménez JM, Griffin WL, Gervilla F, Proenza JA, O'Reilly SY, Pearson NJ (2014) Chromitites in ophiolites: how, where,
656 when, why? Part I. A review and new ideas on the origin and significance of platinum-group minerals. Lithos 189:127-139.
657 https://doi.org/10.1016/j.lithos.2013.10.017
658 Güneş A (2018) Petrology, geochemistry and petrogenesis of isolated dikes from the Tekirova ophiolite. Dissertation, Akdeniz Uni-
659 versity (in Turkish)
660 Güneş A, İlbeyli N, Rasimgil S, Demirbilek M (2021) Petrological and geochemical characteristics of diabase and metasomatised dikes
661 from the Tekirova ophiolite (SW Anatolia, Turkey). Geochemistry 81(3):125767. https://doi.org/10.1016/j.chemer.2021.125767
662 Hanghøj K, Kelemen PB, Hassler D, Godard M (2010) Composition and genesis of depleted mantle peridotites from the Wadi Tayin
663 Massif, Oman ophiolite: major and trace element geochemistry, and Os isotope and PGE systematics. J Petrol 51:201-227.
664 https://doi.org/10.1093/petrology/egp077
665 Hewson RD, Cudahy TJ, Mizuhiko S, Ueda K, Mauger AJ (2005) Seamless geological map generation using ASTER in the Broken
666 Hill-Curnamona Province, Australia. Remote Sens Environ 99:159-172. https://doi.org/10.1016/j.rse.2005.04.025
667 Honarmand M, Shahriari H, Zadeh MH, Ghorbani A (2024) Enhancing Zn-bearing gossans from GeoEye-1 and Landsat 8 OLI data
668 for non-sulphide Zn deposit exploration. Egypt J Remote Sens Space Sci 27(1):93-107. https://doi.org/10.1016/j.ejrs.2024.01.003
669 Juteau T (1975) Les ophiolites des nappes d'Antalya (Taurides occidentales, Turquie): petrologie d'un fragment de l'ancienne croute
670 oceanique tethysienne. Dissertation, Universite de Nancy I
671 Mars JC, Rowan LC (2006) Regional mapping of phyllic- and argillic-altered rocks in the Zagros magmatic arc, Iran, using Advanced
672 Spaceborne Thermal Emission and Reflection Radiometer (ASTER) data and logical operator algorithms. Geosphere 2(3):161-186.
673 https://doi.org/10.1130/GES00044.1
674 Maxwell AE, Warner TA, Fang F (2018) Implementation of machine-learning classification in remote sensing: an applied review. Int
675 J Remote Sens 39(9):2784-2817. https://doi.org/10.1080/01431161.2018.1433343
676 Mountrakis G, Im J, Ogole C (2011) Support vector machines in remote sensing: a review. ISPRS J Photogramm Remote Sens 66(3):247-
677 259. https://doi.org/10.1016/j.isprsjprs.2010.11.001
678 Orynbassarova E, Ahmadi H, Adebiyet B, Bekbotayeva A, Abdullayeva T, Beiranvand Pour A, Ilyassova A, Serikbayeva E, Talgar-
679 bayeva D, Bermukhanova A (2025) Mapping alteration minerals associated with Aktogay porphyry copper mineralization in
680 eastern Kazakhstan using Landsat-8 and ASTER satellite sensors. Minerals 15(3):277. https://doi.org/10.3390/min15030277

Pour AB, Hashim M, Hong JK, Park Y (2018) Lithological and alteration mineral mapping in poorly exposed lithologies using Landsat-8 and ASTER satellite data: north-eastern Graham Land, Antarctic Peninsula. Ore Geol Rev 108:112-133. https://doi.org/10.1016/j.oregeorev.2017.07.018

Rajendran S, Nasir S, Kusky TM (2012) ASTER detection of chromite-bearing mineralized zones in the Semail Ophiolite Massifs of the northern Oman Mountains. Ore Geol Rev 44:121-135. https://doi.org/10.1016/j.oregeorev.2011.09.010

Robertson AHF (1998) Tectonic significance of the Eratosthenes Seamount: a continental fragment in the process of collision with a subduction zone in the eastern Mediterranean (Ocean Drilling Program Leg 160). Tectonophysics 298(1-3):63-82. https://doi.org/10.1016/S0040-1951(98)00178-4

Robertson AHF, Woodcock NH (1980) Strike-slip related sedimentation in the Antalya Complex, SW Turkey. In: Ballance PF, Reading HJ (eds) Sedimentation in oblique-slip mobile zones. Spec Publ Int Assoc Sedimentol, pp 127-145. https://doi.org/10.1002/9781444303735.ch8

Robertson AHF, Woodcock NH (1982) Sedimentary history of the south-western segment of the Mesozoic-Tertiary Antalya continental margin, south-western Turkey. Eclogae Geol Helv 75(3):517-562

Rowan LC, Mars JC, Simpson CJ (2005) Lithologic mapping of the Mordor ultramafic complex using ASTER. Remote Sens Environ 99(1-2):105-126. https://doi.org/10.1016/j.rse.2004.11.021

Sultan M, Arvidson RE, Sturchio NC (1986) Mapping of serpentinites in the Eastern Desert of Egypt by using Landsat thematic mapper data. Geology 14(12):995-999. https://doi.org/10.1130/0091-7613(1986)14<995:MOSITE>2.0.CO;2

Traore M, Wambo JDT, Ndepete CP, Tekin S, Pour AB, Muslim AM (2020) Lithological and alteration mineral mapping for alluvial gold exploration in the south east of Birao area, Central African Republic using Landsat-8 Operational Land Imager (OLI) data. J Afr Earth Sci 170:103933. https://doi.org/10.1016/j.jafrearsci.2020.103933

Traore M, Can T, Tekin S (2022) Mapping carbonate-hosted Pb-Zn mineralization zones in Yahyali Province (Eastern Taurus, Turkey) using ASTER data. Adv Space Res 69(1):266-281. https://doi.org/10.1016/j.asr.2021.07.034

Unal S, Yalcin MG, Ocak S, Yalcin R, Ozmen SF (2018) Computation of gamma radioactivity of natural rocks in the vicinity of Antalya province and its effect on health. Kerntechnik 83(2):112-120. https://doi.org/10.3139/124.110895

Velbel MA (2009) Dissolution of olivine during natural weathering. Geochim Cosmochim Acta 73:6098-6113. https://doi.org/10.1016/j.gca.2009.07.024

Wilson EB (1927) Probable inference, the law of succession, and statistical inference. J Am Stat Assoc 22:209-212. https://doi.org/10.1080/01621459.1927.10502953

Younis MA, Elyaseer MH, Shahin TM et al (2025) Integrated remote sensing and petrological study of garnet-bearing rocks in the Arabian-Nubian Shield: a case study from Wadi Shait-Wadi Gemal area, South Eastern Desert, Egypt. Sci Rep 15:35409. https://doi.org/10.1038/s41598-025-21601-6

Zoheir B, Emam A, Abdel-Wahed M, Soliman N (2019) Multispectral and radar data for the setting of gold mineralization in the South Eastern Desert, Egypt. Remote Sens 11(12):1450. https://doi.org/10.3390/rs11121450